Chapter 8

Electronics for Power and Energy Management

Naser Khosro Pour, François Krummenacher and Maher Kayal

Additional information is available at the end of the chapter

http://dx.doi.org/10.5772/57281

1. Introduction

There is an increasing demand for energy-efficient wireless sensor networks (WSN) in different sensing and monitoring applications. Many autonomous WSN solutions have been deployed in different areas, including health and lifestyle, automotive, smart buildings, predictive maintenance (e.g., of machines and infrastructure) and active RFID tags [1]. For example, miniaturized wireless body area network (WBAN) platforms that can monitor various biological and physiological signals are highly demanded [2]. These WSN platforms face the main technological challenges of miniaturization, autonomy and manufacturing cost [3]. As long lifetime and small form factor requirements of these applications cannot be provided by miniaturized primary batteries, energy harvesting and charging miniaturized rechargeable batteries could be a good solution for realizing autonomous WSNs. These emerging autonomous ultra-low power (ULP) sensors incorporate energy harvesting source, energy storage device and electronic circuits for power management, sensing and communication into a miniaturized system.

The main energy harvesting sources that have been deployed in WSN applications are vibrational, thermal, photovoltaic, and radio frequency (RF) energy sources. Nanoscale energy sources for solar, kinetic and thermal energy harvesting were thoroughly discussed in the previous chapters. As mentioned before, in a kinetic energy harvester, including electrostatic, piezoelectric, and electromagnetic transducers, motion is transduced to electrical power. These transducers have different power throughputs ranging from almost $1\mu W/cm^2$ up to $100\mu W/cm^2$ depending on environmental conditions [1]. The output voltage depends on the transducer type and typically it tends to be too low in the case of electromagnetic transducers and too high in the case of electrostatic transducers [4]. When two junctions that are made of two dissimilar conductors are kept at different temperatures, an open circuit voltage develops

between them based on the seebeck effect that can be harvested by an appropriate thermal energy harvester circuit [5]. Although the source power can reach to 100mW/cm^2 for industrial applications, the temperature gradient and the efficiency are much lower for human body application comparing to machine applications [1]. Ambient RF energy is another source of energy harvesting. Although RF energy harvesting can be very attractive for some applications including RFID tags, for wirelessly powering miniature sensors, either a large area antenna should be used or the RF energy source should be used in close proximity of the sensor node. For example in [6], in order to harvest1.5mW in the target autonomous sensor, a 100 mW RF energy source has to be placed at 20 cm proximity of the sensor. Finally, solar cells are the most widely deployed energy harvesting sources that convert incoming photons into electricity. Solar energy is the most abundant and practical form of ambient energy and miniaturized solar cells are already available in the custom sizes as small as 1mm^2 [7]. Especially for outdoor applications, they are an obvious energy source for autonomous systems, as the source power can reach to 100mW/cm^2. However for Indoor applications, illumination levels are much lower in the order of 100μW/ cm^2. Efficiencies of these energy transducers range from 5–30%, depending on the used material and indoor or outdoor conditions. Thanks to their high efficiencies, solar cells can be good energy sources for miniaturized autonomous wireless sensor nodes, even in the order of a few cubic millimeters size. The energy that harvesting sources provide highly depends on environmental conditions. In many WSN platforms, combinations of different energy harvesting sources have been used to guarantee autonomous operation of the sensor. For example, in [8] both thermal and photovoltaic energy harvesters have been exploited to power an ECG system.

Successful implementation of energy harvesting for WSN applications mainly depends on meeting size, autonomy and cost constraints. Meeting these constraints can be quite challenging and highly depends on the chosen application and data transmission requirements. At present, complex wireless sensor platforms such as iMote [9] have been realized as printed circuit boards (PCB) and cannot be used for realizing millimeter-scale sensors. First of all, bulky batteries are needed to provide the required peak and average power during sensing and data transmission. In addition, most of standard wireless transmission protocols such as Zigbee transceivers [10] require centimeter-scale antennas. In order to replace these bulky batteries by miniaturized energy storage options, not only new materials and architectures such as thin film Li-ION batteries should be developed, but also robust low-power circuits should be developed for sensing and wireless data communication. By using smaller batteries for these low power circuits and developing new wireless transmission methods that require smaller antennas, millimeter-scale wireless sensor will become feasible. These millimeter-scale wireless sensor systems create a lot of new applications, such as continuous monitoring of intraocular pressure (IOP) to detect and track the progression of glaucoma. Current eye pressure measurement techniques are invasive and must be performed at a doctor's office, however by using an implanted sensor, IOP can be logged continuously using a capacitive MEMS sensor and periodically transmitted to a base station to be communicated with the doctor. In [11], an autonomous wireless intraocular pressure monitor microsystem has been presented that incorporates a miniaturized photovoltaic (PV) module, a miniaturized thin film Li-Ion battery and the required electronic circuit for solar energy harvesting, sensor readout

and data communication in a 1.5mm^3 biomedical implant. Since the sensor is implanted in the eye, meeting miniaturization target is crucial; the size of the thin-film battery has been limited to 1mm^2 that has only 1.5uAh capacity.

Although for some WSN applications such as implanted biomedical sensors and monitoring infrastructures, cost is not the main issue, however for most of other applications, current harvesting technologies are still far too expensive. In fact, low sensor cost is vital for the mass deployment of autonomous sensors in smart dust applications. A possible route to realize less expensive sensors is the use of MEMS technology for manufacturing. The devices could then be made on a wafer basis in a batch mode, thereby greatly reducing the size and the cost. But reducing the size of the sensor reduces not only the cost but also the harvested energy. In order to meet stringent power requirements of these sensors, the total power consumption of the WSN platform should be minimized by proper circuit design of all power-hungry components, including wireless transceiver, sensor frontend circuit, processor, and memory blocks. In addition, as miniaturized energy harvesters can supply approximately 10 μW–1 mW, designing efficient power management circuits is also very important and can be quite challenging. In this chapter, we will focus on power management circuits for solar energy harvesting. Another major challenge for realizing millimeter-scale wireless sensors is antenna miniaturization. Low-frequency radios suffer from poor transmission distances while high-frequency radios require high-bandwidth high-power circuits [12].

The system level design of the power management circuit starts by selecting an appropriate energy harvesting source and energy storage device, and the circuit is designed to harvest the maximum energy from the energy harvesting source and store in the energy storage option with maximum efficiency. In fact, as harvested energy is intermittent, either a rechargeable microbattery or a supercapacitor should be used as energy storage device for reliable operation of electronic circuits that are used for power management, sensor interfacing and wireless data transmission. In fact, usually the power that is delivered by the harvester is less than the peak power that the sensor requires during sensing or radio communication. In addition, although the average power that energy harvesting source provides should be higher than the average power consumption of the sensor, a temporary mismatch between power generation and consumption could exist and an energy storage device is needed for continuous operation.

Although the main factor for selecting an appropriate PV module is the power that it can provide in different lighting conditions, other characteristics of the PV module, such as open circuit voltage, short circuit current and maximum power point of the PV module, should be also considered to design a highly efficient solar energy harvester. A PV module provides a DC voltage that highly depends on the illumination level and temperature and can be different from the nominal voltage of the target NiMH or Li-ION battery. In addition, the battery voltage changes from its nominal voltage during battery charging and discharging. As the DC voltage of the PV module differs from the voltage of the target battery, different inductive [13] and switched-capacitor (SC) [14, 15] DC-DC converters have been proposed to harvest energy from a miniaturized PV module to charge a battery. Typically these DC-DC converters either use external capacitors or inductors or they operate at high frequencies and use sophisticated control circuits to reach high efficiency in the fully integrated DC-DC converters. However,

by using higher frequencies or deploying complex control circuits, the power consumption of power management circuit Is increased and a high efficiency is not achievable under reduced illumination levels when input power is only a few micro-watts. In the direct charging approach [16], the battery is connected to the PV module through a switch, similar to low dropout regulators. However instead of using error amplifiers [17], low power SC circuits have been used to control the switch. By properly matching the PV module and the target battery, this approach achieves a very high efficiency during charging either NiMH or Li-ION batteries [16, 18]. In addition, as neither inductor nor large capacitors have been used, the die area is much smaller comparing to conventional SC or inductive DC-DC converters.

In addition to charging the target battery, since under reduced light intensity, harvested energy from the PV module may be lower than the power consumption of the microsystem, the energy management circuit should dynamically reduce power consumption of the sensor to avoid complete discharge of the battery. As a result, the microsystem can continue its autonomous operation at a lower speed. The power management circuit can measure the remaining charge of the target rechargeable microbattery or supercapacitor and scales the power consumption of the microsystem up or down according to the energy stored in the battery. In this chapter, first of all, all main blocks of the solar energy harvester, including the power management circuit, energy harvesting source and energy storage device will be discussed thoroughly and after that, the proposed circuit will be used to power a miniaturized autonomous sensor. In fact, size and power requirements of a WSN platform highly depend on the target application and how the measurement results should be processed and communicated with a base station or other target sensors. The target sensor is an autonomous hydrogen gas sensor [19]. In fact, as the use of hydrogen fuels becomes more common, an increased demand for low cost miniaturized hydrogen sensors is expected. Palladium (Pd) nanowire hydrogen sensors, which can be used at room temperature, have good sensitivity thanks to their large surface-to-volume ratio while maintaining low power operation and small form factor [20]. Therefore, these miniaturized sensors are good candidates for ultra-low power (ULP) hydrogen sensing. The readout circuit should measure the change in conductivity of Pd nanowires upon hydrogen exposure [21]. As these nanowires have an undesired thermal cross-sensitivity, temperature is also measured and further compensated during sensor calibration, for accurate measurement of hydrogen concentration [21]. In [39], a miniaturized autonomous sensor has been presented that uses nanowire materials to realize the sensor and the energy harvesting source. The total size of this WSN platform is mainly constrained by the battery and wireless transceiver.

2. Energy storage option

Selecting an appropriate energy storage device is the first step in designing an energy harvester circuit, and the power management circuit should be designed with the target of optimizing the overall power efficiency, based on the selected energy storage device. Millimeter-scale sensors that rely on micro-power energy harvesting, typically have additional stringent constraints on die area and usage of external components. Although the target sensor may

http://dx.doi.org/10.5772/57281

consume only a few μA on average for sensing and data transmission, the peak power consumption during wireless data transmission is typically much higher. For example, the TZ1053 wireless transceiver consumes 3.3 mA and 2.8 mA during data transmission and reception [22]. Wireless transceivers that are compatible with standard protocols such as CC2520 that uses Zigbee [23] or CC2570 that uses ANT protocol [24] consume even more during data transmission or reception. Miniaturized supercapacitors, NiMH and Li-ION microbatteries are different solutions that have been used in many wireless sensing platforms. The battery should have enough capacity to provide enough power for a few hours' operation of the sensor, even without energy harvesting. In addition to size and capacity, other characteristics, such as peak discharge current, nominal operating voltage, end-of-charge voltage (V_{EOC}), end-of-discharge voltage (V_{EOD}), cycle life and self-leakage should be considered to design energy-efficient sensors that rely on energy harvesting source. Although tiny supercapacitors, such as GZ115F of CAP-XX [25], can be charged and discharged using much higher currents and have much longer cycle lives in comparison with the rechargeable batteries, they have some disadvantages that make them inappropriate for some WSN platforms including miniaturized autonomous sensors that are normally idle for a very short duty cycle during their operation. The main disadvantage of supercapacitors is their high leakage currents that can be even larger than the current provided by the PV cell under reduced illumination level. In addition, they have much lower energy capacity compared with rechargeable batteries of similar sizes which can provide enough power for continuous operation of the sensor when the energy harvesting source is missing for a few hours. Among lithium-based batteries, state-of-the-art thin film lithium batteries, such as MEC220 of Infinite Power Solutions [26] or CBC050 of Cymbet [27], are a promising technology for integrated energy storage. These microbatteries can be used instead of bulky batteries for millimeter-size WSN platforms as miniaturized batteries are already available in the custom sizes as small as $1mm^2$ [27]. These batteries, that have only 200μm thickness, can be used as bare dies to be embedded into modules directly or co-packaged with other integrated circuits. In addition to small size and low thickness, these microbatteries have very low self-leakage, long cycle lives and high discharge currents that make them ideal energy storage options for autonomous wireless sensors with low operation duty cycles. Table 1, compares the main characteristics of this battery with MEC220 thin film lithium battery and GZ115F supercapacitor. This thin film Li-Ion battery supports up to 10000 recharge cycles as can be seen in this table. The charge loss of this battery can be as small as 2% per year in room temperature. Although the capacity of this battery is only 400μAh, it can support a high pulse discharge current of 15mA. The main disadvantage of these batteries is their high nominal voltage levels and their higher cost comparing to conventional NiMH and Li/ION batteries. As thin film lithium batteries have nominal voltages of more than 3.8 V, additional DC-DC converters are required to use these batteries for ULP applications. NiMH microbatteries have a nominal voltage of 1.2 V and can provide relatively high capacity and discharge current. For example, Varta V6HR microbattery [28] has a large nominal capacity of 6.2 mAh and can provide a peak discharge current of 18 mA, while its diameter and height are 6.8 mm and 2.15 mm, respectively. The miniaturized gas sensor that has been proposed in [21] uses this battery as the energy storage option.

Energy Storage Option/ Specification	GZ115F of CAP-XX [24]	MEC220 of Infinite Power Solutions [25]	V6HR of Varta [27]
Technology	Supercapacitor	Thin film battery	NiMH battery
Nominal Voltage	2.3V	4.1V	1.2V
Size	20X15X1.25 mm^3	25.4X25.4X0.17 mm^3	D: 6.8mm, H: 2.15mm
Energy Capacity	4 μAh	400 μAh	6,200 μAh
Peak Discharge Current	30A	15mA	18mA
Cycle life	30,000+ hours	10,000	1,000

Table 1. Comparing energy storage options

Selecting appropriate energy storage option highly depends on the size, cost, wireless communication and autonomy constraints in the target WSN platform. At present, thin film Li-ION batteries can be as small as $1mm^2$, but these tiny batteries cannot provide enough discharge current for standard wireless communication protocols. In addition, these batteries are not appropriate for low-cost applications due to their much higher prices comparing to conventional NiMH or Li-ION batteries. If standard wireless communication protocols are supposed to be used in a low-cost application, conventional NiMH or Li-ION microbatteries are still the best options. These batteries should be able to provide required impulse current during data transmission. Finally autonomy requirements should be considered to select a battery with enough energy capacity to provide enough energy during the time interval that energy harvesting source is missing. NiMH microbatteries have been widely used as energy source for different applications and typically have very low prices. As can be seen in this table, Varta V6HR has a relatively high capacity and discharge currents, while its 1.2 V nominal voltage can be an additional advantage in ULP applications. If in the target sensor, all electronic circuits, including the external wireless transceiver, can operate with a sub-1.2 V supply voltage, additional step-down or step-up circuits are not required. The main disadvantage of Varta V6HR NiMH battery in comparison with MEC220 thin film lithium battery is its lower cycle life and higher discharge current. This battery loses almost 20% of its charge during the first month. The main disadvantage of Varta V6HR NiMH battery in comparison with GZ115F is its lower discharge current and shorter cycle life. On the contrary its capacity is much higher and the leakage current is much less than GZ115F. Although supercapacitors have low energy capacity and high leakage current that makes them inappropriate for miniaturized energy harvesting applications where harvested energy is in the order of 10 μW–100 μW, thanks to their high discharge current and their long cycle life, they can be ideal candidates for complex WSN platforms with higher input powers. These supercapacitors can be used as energy buffers besides the rechargeable batteries to provide impulse currents.

3. Solar energy harvester

The solar energy harvester circuit should harvest energy from input solar cells and store it in the target rechargeable battery with the maximum end-to-end efficiency. The main tasks of a

solar energy harvester block are battery charging, battery management and energy management. In order to achieve high efficiency, the main characteristics of the PV module, such as open circuit voltage, short circuit current and maximum output power should be considered. A single solar cell can be modeled as in Figure 1 [29]. The open circuit voltage of a miniaturized solar cell is only a few hundred millivolts and if it is supposed to be used to charge a NiMH battery, either inductive boost DC-DC converters or step-up SC DC-DC converters should be used and direct charging approach cannot be deployed. However single solar cells can be connected in series to provide higher DC voltages. In direct charging approach, an appropriate number of solar cells should be used in series to provide sufficient DC voltage. In [21] four miniaturized nanowire solar cells [30] have been connected in series to charge a NiMH microbattery, while to charge a thin film Li-ION battery ten solar cells should be used in a series configuration [18].

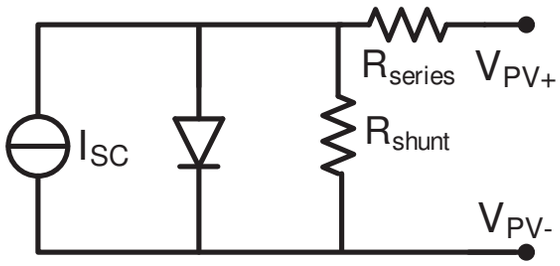

Figure 1. Circuit model of a single solar cell

The block diagram of a miniaturized autonomous sensor that uses direct charging method to charge a NiMH battery is depicted in Figure 2. In the solar energy harvester, the battery voltage (V_{bat}) is compared with the open circuit voltage of the PV module (V_{pv}) using a dynamic comparator, and if it is lower, the battery is connected to the PV module to store harvested energy. If V_{pv} drops below V_{bat}, the switch between V_{pv} and V_{bat} is kept turned off to avoid battery discharge through the PV module. In this approach, the maximum power point voltage (V_{mpp}) of the PV module should be close to the V_{EOC} of the battery to achieve high efficiency. Although P_{mpp} and I_{SC} of the PV module changes considerably in different lightning conditions, V_{oc} and V_{mpp} of the PV module does not change significantly. In Figure 3, the deliverable power of a PV module that uses four solar cells in series has been simulated at different illumination levels using the electrical model of the solar cell [19]. This PV module has a total area of 28 mm^2 and can provide a maximum power P_{mpp} of 2.88 mW in AM1.5 illumination. In AM1.5, solar intensity is almost 1 mW/mm^2. At 10% of AM1.5, although the deliverable power is reduced by roughly the factor of 10, V_{oc} just drops from 2.35 V to 1.95 V.

The second main task of the energy harvester circuit is battery management. In miniaturized sensors that rely on energy harvesting, as the charging current is limited by the PV module, normally the battery is charged in either standard or trickle charging modes, depending on the illumination conditions and capacity of the battery and there is no need to limit charging current [28]. In trickle charging mode, the battery is charged by a small current, and it can be

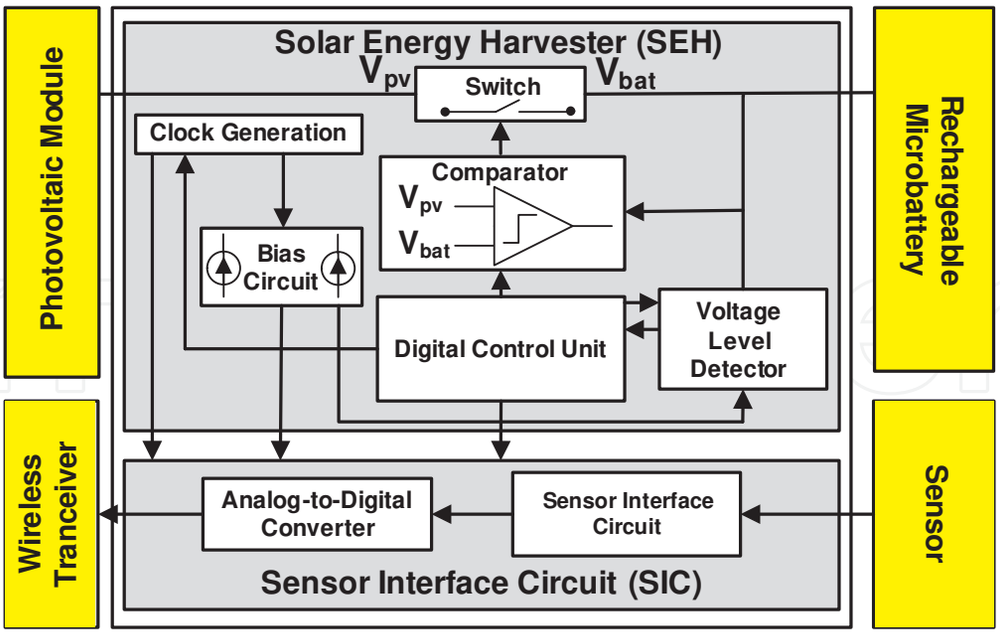

Figure 2. Block diagram of the proposed hydrogen gas sensor

continuously charged, even after reaching V_{EOC}. For example in Varta V6HR, if charging current is less than 3% of its 6mAh energy capacity or equivalently 180μA, the battery is charged in trickle charging mode. Trickle charging limit is normally a function of the energy capacity of the battery and larger batteries have higher charging limits. When battery is charged by a charging current that is higher than this trickle charging limit, the battery charging should be stopped after reaching V_{EOC} to avoid permanent damage to the battery. In addition, to avoid full discharge of the battery that reduces the cycle life of the battery, the battery should be disconnected from the sensor when the battery voltage drops to V_{EOD}. As a result, the battery management unit should detect V_{EOC} and V_{EOD} voltage levels to avoid overdischarge or overcharge of the battery [16]. Finally, the last task of the energy harvester circuit is energy management. Since, under reduced light intensity, the power delivered by the PV module may be lower than the average power consumption of the sensor, the energy harvester circuit should reduce power consumption of the microsystem to avoid full discharge of the battery during this period. Under reduced light intensity, the microsystem continues its autonomous operation at a lower speed and with a lower duty cycle. The energy management circuit can measure the remaining charge of the target battery and scales the power consumption of the microsystem up or down according to the measurement results. In order to reduce the power consumption and speed of digital circuits, the operating frequency is scaled down and the data transceiver is activated by a lower duty cycle. Bias currents are also scaled down to reduce power consumption and the speed of analog circuits. In order to reliably estimate the energy stored in the battery, battery voltage is measured when the battery is discharged by a high discharge current. As harvested solar energy may be as small as a few micro-watts under reduced light intensities, the power consumption of the energy harvester circuit should not be higher than a few hundred nanowatts to have high efficiency during these periods. As

neither Vpv nor Vbat changes rapidly, comparator and voltage level detector blocks are activated every few seconds to minimize average power consumption [19].

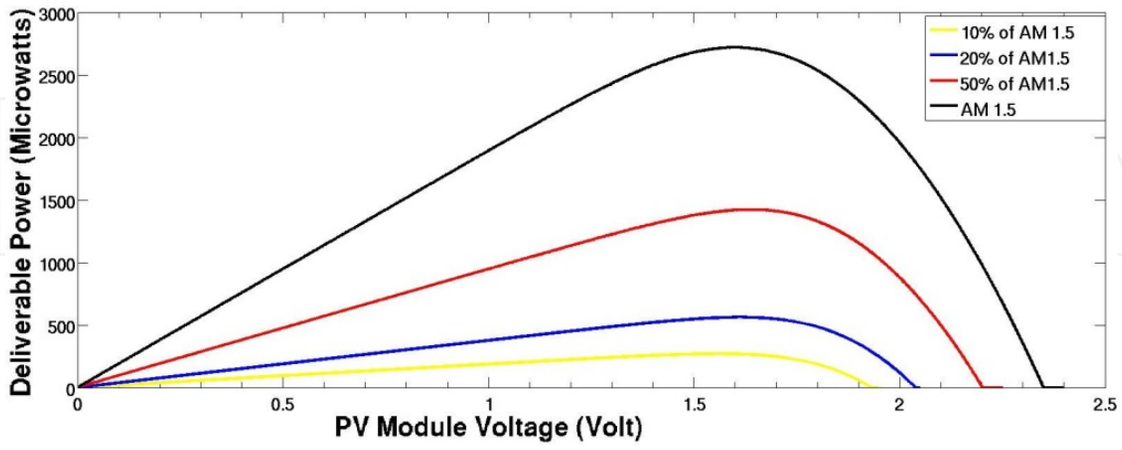

Figure 3. Deliverable power of the PV module in different lightning condition [19]

The dynamic comparator and required control signals can be seen in Figure 4. After turning off the switch between V_{pv} and V_{bat}, the first inverting gain stage gets reset by activating the reset control signal, to establish a common mode voltage of V_{cm} at the V_{C_Top} node. Meanwhile, V_{C_Bot} is connected to V_{pv} by activating the Sample_V_{pv} control signal, and the difference between V_{pv} and V_{cm} is sampled on the sampling capacitor. In the next step, by deactivating the reset and activating Sample_V_{bat} control signal, V_{C_Bot} is connected to V_{bat}, and as a result, V_{C_Top} changes to $V_{cm} + (V_{bat} - V_{pv})$. Outputs of the first and second gain stages (V_{o1} and V_{o2}) change according to the new V_{C_Top}, and V_{o2} is latched and stored as V_{Comp}, by enabling the latch_enable control signal. If V_{Comp} gets 1, it means that V_{bat} is higher than V_{pv}, and the switch should be kept turned off to avoid battery discharge, but if V_{Comp} gets 0, the PV module starts to charge the battery by turning on the switch. After the switch is turned on, V_{pv} will follow V_{bat} during battery charging.

As the operating voltage of the PV module is determined by the battery, end-to-end efficiency from the PV module to the battery is reduced when the battery voltage diverges from the V_{mpp} of the PV module during battery charging. Different maximum power point tracking (MPPT) strategies have been deployed in energy harvesting applications to maximize the amount of harvested energy. As the V_{mpp} of the PV module varies with incident light conditions, an efficient MPPT scheme ensures that the maximum power is extracted from a PV module at any given time. Many complex and accurate MPPT schemes have been investigated for large solar harvesting systems [31]; however, when the PV module is small and can only provide a few micro-watts under reduced light intensity, only low-overhead schemes that incur very little power overhead can be good candidates. Several low-overhead MPPT approaches, including fractional open-circuit voltage (FOC), fractional short circuit current (FSC) and hill-climbing techniques, can be deployed in inductive and SC DC-DC converters [32]. In direct charging V_{pv} always follows V_{bat} and no MPPT scheme can be deployed. Nevertheless, it can achieve even higher end-to-end efficiency than competing SC and inductive DC-DC converters. In [16], end-to-end efficiency from the PV module to the battery has been simulated at different illumina-

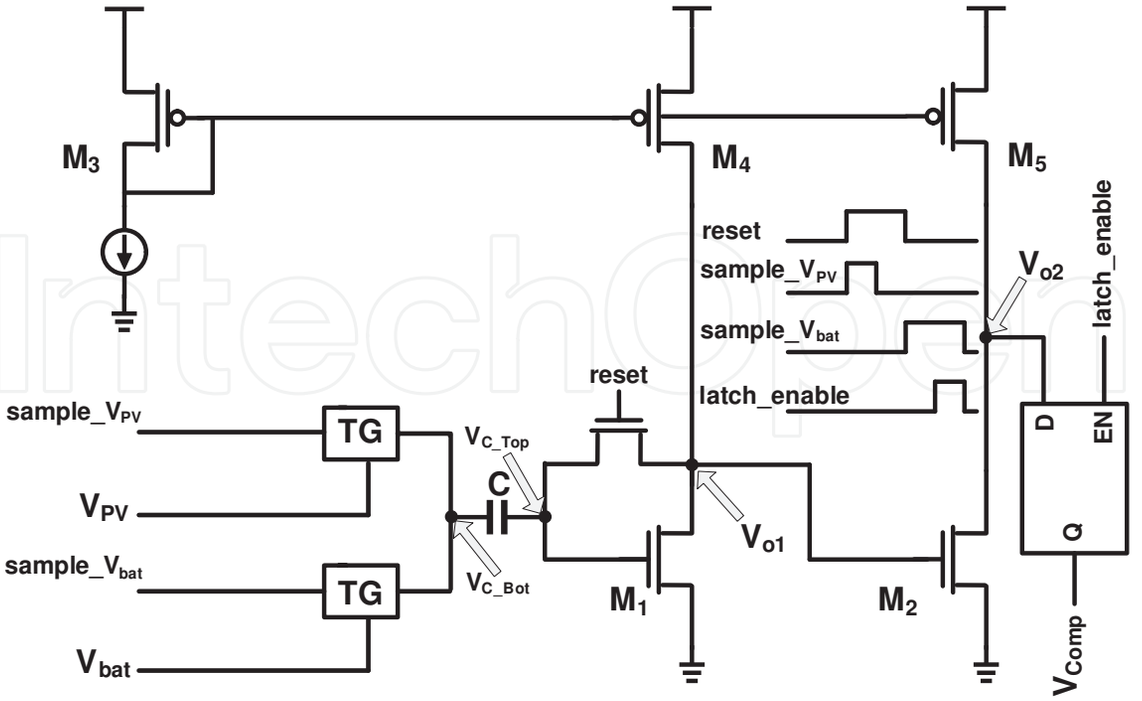

Figure 4. Circuit diagram of dynamic comparator [19]

tion levels. As can be seen in Figure 5a, the miniaturized PV module that has been used as energy harvesting source can provide maximum power of 77.1μW at 1.33V under AM1.5 illumination. The efficiency reaches to the minimum value of 76.9% when the battery is fully discharged. Starting from a fully discharged NiMH battery at V_{POR} and charging it up to fully charged state at V_{EOC}, the average end-to-end efficiency during charging process is 90.6%. In Figure 5b, although illumination is reduced by a factor of 10 and the maximum input power is only 6.36μW, the average efficiency during charging process is still 85.2%. In fact, since the voltage of the PV module does not change significantly at different lighting conditions, the MPP of PV module is still close to nominal voltage of battery and a high end-to-end efficiency from PV module to the battery is achievable without any MPP tracking.

Table 2 compares the simulated performance of the circuit we described with state of the art SC and inductive DC-DC converters that had been previously used for micro power solar energy harvesting. The proposed power management system, achieves better end-to-end efficiency in comparison to these circuits. In addition, as neither inductor nor large capacitors have been used in this architecture, the die area is minimized. Finally as high quality capacitors or inductors are not required, the circuit can be easily realized in different technologies.

When the target rechargeable battery is discharged by a high current, the battery voltage drops and the voltage drop depends on the remaining charge of the battery. For example, when the V6HR NiMH microbattery is fully charged, the battery voltage is close to V_{EOC}; as the battery is discharged by a low current, V_{bat} drops to its nominal value and remains almost constant, up to getting close to the fully discharged state. However, if the battery is discharged by a high current, as can be seen in the discharge curve of the battery in Figure 6 [28], V_{bat} drops

http://dx.doi.org/10.5772/57281

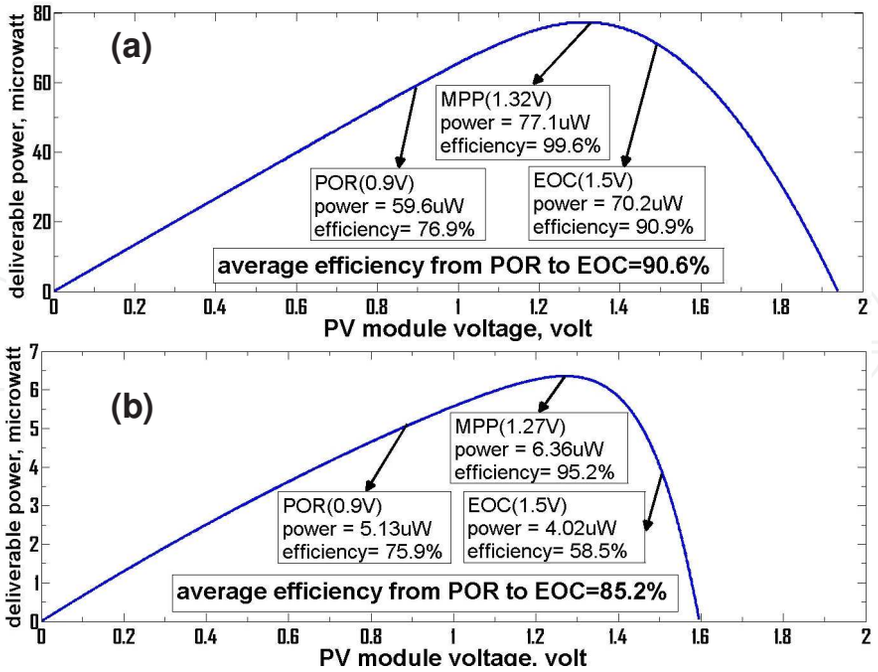

Figure 5. Efficiency of power management system, under simulated AM 1.5 illumination (Figure 5a), under simulated 10% light intensity (Figure 5b)

immediately and voltage drop depends on the remaining charge of the battery. During wireless data transmission, the battery is discharged by a high current, close to 5 CA (C being the 1 hour charge or discharge current). As can be seen in Figure 6, if discharge capacity is less than 20%, V_{bat} is higher than 1.1 V during this period; however, if discharge capacity is higher than 20%, V_{bat} drops from 1.1 V down to 900 mV, depending on the remaining charge of the battery. In our circuit, the battery voltage is detected during this period to accurately estimate the energy stored in the battery. Depending on the detected V_{bat}, the power-performance of the integrated electronic circuits and operation duty cycle of the wireless transceiver are reconfigured to guarantee autonomous operation of the sensor. If V_{bat} is high enough, the sensor can operate at its highest performance: solar energy harvester and sensor interface circuits work at their highest speed, and measurement results are sent to the base station every 10 seconds. If V_{bat} is not high enough, the sensor interface circuit and wireless transceiver are activated with a lower duty cycle to minimize total power consumption of the sensor. If V_{bat} is close to V_{EOD}, these blocks should be deactivated temporarily to avoid full discharge of the battery. Battery voltage can be detected during this period to accurately estimate the energy stored in the battery. Depending on the detected V_{bat}, the power-performance of the integrated electronic circuits and operation duty cycle of the wireless transceiver can be reconfigured to guarantee autonomous operation of the sensor. If V_{bat} is high enough, the sensor can operate at its highest performance: solar energy harvester and sensor interface circuits work at their highest speed, and measurement results are sent to the base station every 10 seconds. If V_{bat} is not high enough, the sensor interface circuit and wireless transceiver are activated with a lower duty cycle to minimize total power consumption of the sensor. If V_{bat} is close to V_{EOD}, these blocks should get deactivated temporarily to avoid full discharge of the battery.

	[13]	[14]	[15]	[16]
process	**0.25µm CMOS**	**0.35µm CMOS**	**0.35µm CMOS**	**0.18µm CMOS**
input voltage (V)	0.5~2	2.1~3.5	1~2.7	0.9~2
output voltage (V)	0~5	3.6~4.4	2	0.9~1.5
power throughput	5µW ~10mW	<780µW	0 ~80µW	0~80µW
controller power	2.4µW ~3.5µW	>10µW	450nW ~850nW	<300nW
end-to-end efficiency	70%	67%	86%	90%

Table 2. Performance comparison between different solar energy harvesters [16]

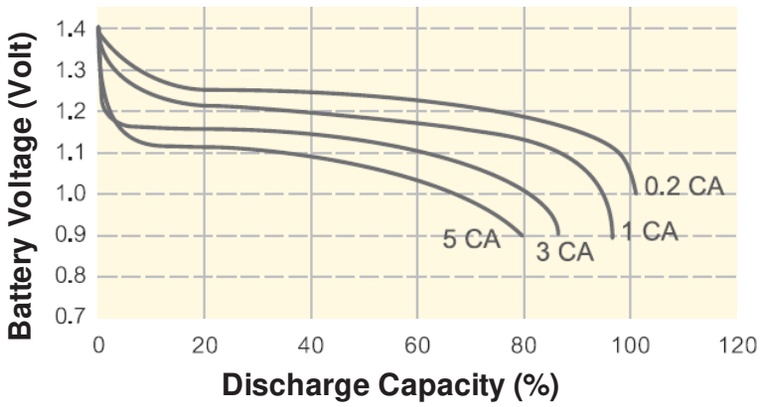

Figure 6. Typical discharge curves of the target NiMH microbattery at room temperature [28]

The voltage level detector (LD) in Figure 7 can be used to determine the battery voltage level [16]. After circuit startup, the battery voltage is checked to make sure that it is more than the end of discharge threshold voltage (V_{EOD}) and can power up the circuit. If V_{bat} is less than V_{EOD}, it means that the battery is fully discharged and cannot provide enough power for the electronic circuits. In this situation, the PV module continuously charges the battery by keeping the switch closed. As soon as V_{bat} passes V_{EOD}, LD starts its normal operation, comparing V_{bat} with specified threshold voltages in a timely manner and updating the V_{bat_level} as a result. In order to generate a bandgap reference voltage, 25 substrate PNP transistors have been used as Q_1 and Q_2 in a common-centroid layout [18]. These transistors are biased with a 100 nA current source to generate V_{BE1} and V_{BE2} in non-overlapping Φ_1 and Φ_2 phases, and the SC circuit sums up V_{BE1} and (V_{BE1}- V_{BE2}) with appropriate coefficients. When V_{bat} reaches V_{EOC}, the switch between the PV module and the battery is turned off to avoid overcharge of the battery.

The SC circuit of Figure 7 operates using non-overlapping clock signals Φ1 and Φ2 and detects when V_{bat} passes the V_L specified in Equation (1) by setting the V_{bat_level} output. Required command signals and status of the switches during Φ_1 phase, can be seen in this figure. In this phase, V_{BE1} is applied to bottom plate of αC and βC capacitors, while bottom plate of γC

http://dx.doi.org/10.5772/57281

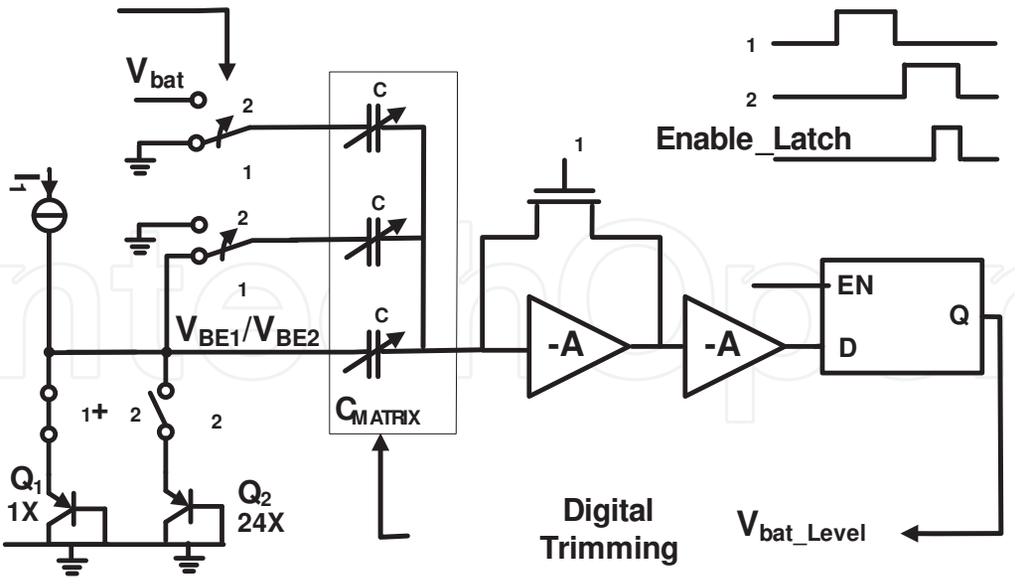

Figure 7. Circuit diagram of voltage level detector [19]

capacitor is grounded. The first inverter gain is reset during this period to establish a fixed common mode voltage for αC, βC and γC capacitors during this period. In phase Φ_2, V_{BE2} is applied to the bottom plate of αC capacitor, while bottom plates of βC and γC capacitors are connected to ground and V_{bat} respectively. As a result the voltage of the top plates of αC, βC and γC capacitors change and this change is amplified by two inverting gain stages and by enabling "Enable_Latch" control signal during phase Φ_2, V_{bat_level} output is updated. By using a variable γC capacitor, different voltage levels between V_{EOD} and V_{EOC} can be detected to estimate the remaining charge of the battery. In Equation (1), α, β and γ coefficients are the ratios of tunable αC, βC and γC capacitors. These variable capacitors have been implemented using a matrix of 10 fF metal-insulator-metal (MIM) capacitors that have been used as unity capacitors.

$$V_L = [\alpha \times (V_{BE1} - V_{BE2}) + \beta \times V_{BE1}] / (\gamma) = V_{ref} / (\gamma) \quad (1)$$

As V_{BE1} is complementary to absolute temperature (CTAT) and (V_{BE1}- V_{BE2}) is proportional to absolute temperature (PTAT), different CTAT, PTAT or temperature-independent reference voltages (V_{ref}) can be built by proper selection of αC and βC capacitors. After that, by modifying the γC capacitor, target voltage levels can be detected. As can be seen in Table 3, by modifying βC and γC capacitors, different battery voltages, starting from V_{EOD} of 0.9 V up to V_{EOC} of 1.5 V, can be detected. In order to have a bandgap temperature-independent voltage reference, αC should be modified according to the selected βC capacitor. By detecting the battery voltage between 900 mV and 1.1 V, the remaining charge of the battery can be estimated according to the discharge curve of the battery in Figure 6. Similar circuit architecture can be used to detect battery voltage of thin film Li-ION batteries [18]. The same bandgap reference can be used as reference voltage.

Voltage Level (V_L)	αC Capacitor	βC Capacitor	γC Capacitor
907mV(V_{EOD})	170fF	1230fF	230fF
947mV(V_{L0})	170fF	1230fF	220fF
1002mV(V_{L1})	180fF	1300fF	220fF
1051mV(V_{L2})	180fF	1300fF	210fF
1104mV(V_{L3})	190fF	1370fF	210fF
1509mV(V_{EOC})	160fF	1160fF	130fF

Table 3. Detected voltage levels in voltage level detector

After measuring V_{bat} and estimating the energy stored in the battery, the operating frequency of digital circuits and bias currents of analog circuits are reconfigured according to the remaining charge of the battery. In the current-starved ring oscillator in Figure 8a, the frequency is determined by R_L and C_L and can be specified as Equation (2). In Equation (2), K_1 is a constant value that depends on the number of inverter stages in the ring oscillator [33]. The left part of this oscillator is a current mirror that makes the inverter ring biased with a total current identical to the one flowing through RL resistor. This total current is split to charge and discharge all load capacitors. Capacitor C1 is used for decoupling the inverter ring supply voltage and does not participate in the time-constant of the oscillator circuit. By using a digital resistive trimming network to modify R_L, F_{osc} is reconfigured by an energy harvesting circuit, according to the measured V_{bat}.

$$F_{osc} = K_1 / (R_L \times C_L) \tag{2}$$

In addition to a fixed 10 nA beta-multiplier (BM) current reference that has been used to provide the required bias current for a solar energy harvester, a switched-capacitor beta-multiplier (SCBM) current source has been designed to generate frequency-proportional bias currents. In this circuit, which can be seen in Figure 6b, SC resistors have been used instead of regular resistors to generate frequency-proportional bias currents [34]. For example, I_{ADC} can be specified as in (3):

$$I_{ADC} = K_1 \times K_2 \times F_{osc} \times (C_3 + C_4) \tag{3}$$

In Equation (3), K_1 and K_2 are constant values that depend on the ratio between the widths of transistors in Figure 8b. K_1 depends on the ratio between M_7 and M_4, and K_2 depends on the ratio between M_5 and M_6. The current ripple of I_{bias} is minimized by using a large decoupling capacitor, C_2, and two complementary branches charging and discharging C_3 and C_4 capacitors in non-overlapping $Ø_1$ and $Ø_2$ clock phases with F_{osc} frequency [34]. As F_{osc} is determined by the oscillator, I_{bias} scales dynamically by changing the frequency of the oscillator. In addition, this current source can be easily deactivated by turning off the $Ø_1$ and $Ø_2$ clocks.

http://dx.doi.org/10.5772/57281

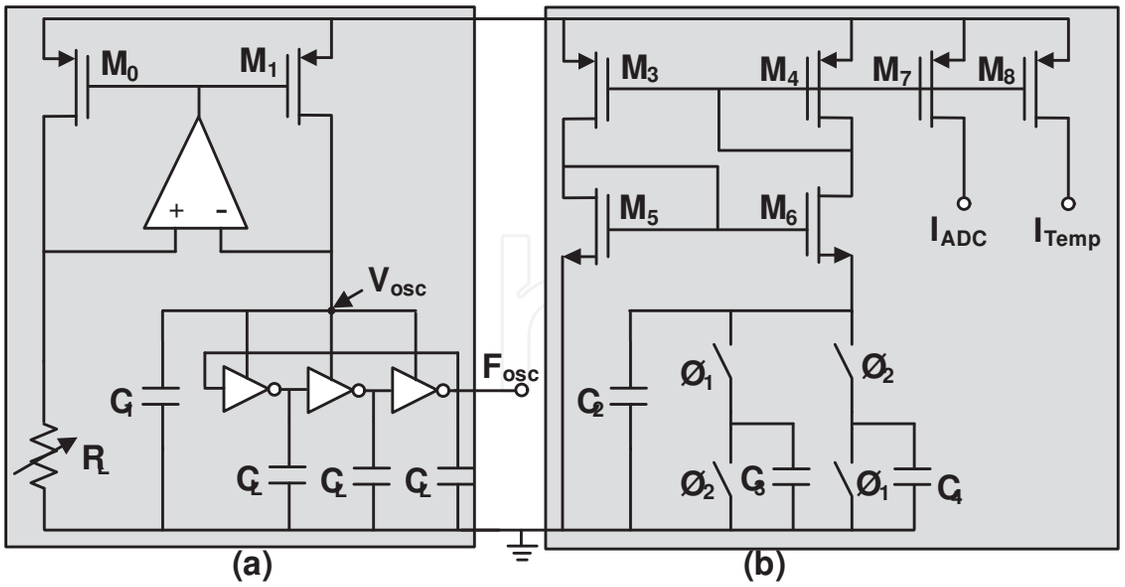

Figure 8. Reconfigurable current-starved ring oscillator (Figure 8a), Switched- capacitor beta-multiplier (SCBM) current source (Figure 8b) [19]

In ultra-low power analog circuits, such as the discrete time incremental ADC that has been used in [21], bias currents should be high enough to guarantee correct operation at the target operating frequency. Bias currents that are generated by SCBM can be used for the sensor interface circuit. If V_{bat} is low, F_{osc} is decreased to reduce the power consumption of digital circuits in the ADC. When the system is operating at a lower frequency, lower bias currents can be used to reduce the power consumption of analog circuits in the sensor interface circuit. By using these frequency-proportional bias currents, power consumption of the sensor can be scaled down dynamically by reducing F_{osc}.

The comparator and LD blocks can be activated in a timely manner, to check the charging status of the battery. As neither V_{bat} nor V_{pv} change rapidly, these blocks are activated every few seconds to minimize their average power consumption. After activating each block, a digital control unit (DCU) generates the required control signals for related SC circuits. The power consumption of DCU is mainly determined by the low frequency counter that activates the comparator and LD in a timely manner. Although comparator and LD blocks consume considerable power during their active time, nevertheless, as they are activated every few seconds, their average power consumption is negligible. The simulated total power consumption of the energy harvester circuit is mainly determined by the clock generator, bias circuit and DCU blocks, which are always active.

4. Wireless transceiver and sensor interface

Emerging wireless sensors that are powered by micro-power energy harvesting sources have more stringent energy requirements compared to traditional wireless sensors. Apart from

minimizing the total power consumption of the sensor, which is mainly achieved by duty cycling operation of the sensor, they should have low peak power and ultra-low standby current. Low peak power ensures that miniaturized batteries with limited peak discharge currents can be used to power up the circuit. Ultra-low standby current guarantees that the average power consumption of the sensor can be minimized by heavily duty cycling sensing and data transmission. The main factors impacting power consumption of a wireless transceiver are supply voltage, carrier frequency and receiver sensitivity. The power consumption of transceiver can be reduced by operating at lower supply voltages. Although most of the wireless transceivers work with at least 1.8 V supply voltage, ultra-low power wireless transceivers with sub-1.2 V voltage, such as TZ1053 [22] or ZL70250 [35], are more suited to miniaturized energy harvesting application, thanks to their lower power consumption during data transmission and reception. These transceivers operate at sub-1 GHz frequency bands and have much lower peak-power and standby power, compared to state-of-the-art 2.4 GHz transceivers.

The second important factor is the carrier frequency. Some of the factors that affect choice of carrier frequency are operation range, power consumption, transmission data rates and antenna size. Although 2.4 GHz protocols, such as Zigbee, have been used extensively for wireless sensing applications, sub-1 GHz wireless systems offer several advantages for ultra-low power, low data rate applications. These transceivers have less power consumption for the same operating range, thanks to reduced attenuation rates and blocking effects at lower frequencies. Besides requiring higher power for the same link budget, higher traffic in the 2.4 GHz frequency band increases the interference in this frequency band. Finally, receiver sensitivity also affects the power efficiency. A narrower bandwidth creates higher receiver sensitivity and allows efficient operation at lower transmission rates. Overall, all radio circuits running at higher frequencies, including low-noise amplifiers, power amplifiers, mixers and synthesizers, need more current to achieve the same performance as lower frequencies do. Sub-1 GHz transceivers have some disadvantages, such as larger size of antennas and lower data rates, but overall, they are more suited for our application. A higher data rate can improve the energy efficiency (energy per bit) of the transceiver for high bandwidth applications with large data payloads. In fact, overall power consumption of a wireless transceiver is not only a factor of physical layer items, such as radio architecture, carrier frequency and antenna choice, but is also a function of the amount of time that the radio needs to run in order to transport the payload data over the air. Transmission time depends on the data rate and the protocol overhead to establish and maintain the communication link. For example, a Zigbee transceiver that has a 250 Kbps data rate can send 1 MB of data almost five-times faster than a TZ1053 that has a 50 kbps data rate. However, in ultra-low power applications, typically, data payloads are small and a 50 kbps data rate is more than enough. As standard protocols, e.g., Zigbee or Bluetooth, offer highly sophisticated link and network layers and have a large protocol overhead, they are not very efficient for sending small data payloads.

Miniaturization of WSN platforms highly depends on the chosen application, in addition to using appropriate wireless transceiver. In fact, in some WSN platforms, minimizing the power consumption of the sensor interface circuit can be quite challenging. A miniaturized Pd

http://dx.doi.org/10.5772/57281

nanowire grid fabricated on a silicon wafer has been used for hydrogen gas sensing. Each grid consists of 14 Pd nanowires, half of which are covered with a passivation layer to prevent hydrogen from reaching the nanowire [36]. These coated nanowires, which are only sensitive to temperature, have been used as reference nanowires, while the remaining nanowires, which are sensitive to both temperature and H_2 concentration, have been used as sensing nanowires. The sensor interface circuit of Figure 9 measures the conductance change of the sensing nanowires in comparison to the reference nanowires. In addition to eliminating the effects of temperature by first order, the measurement is only sensitive to the ratio of conductance of nanowires, instead of their absolute values, and as a result, a higher accuracy is achievable. Although the temperature effect is eliminated by first order, there are still second order effects, as the temperature coefficient of nanowire resistance changes according to H_2 concentration. In order to compensate this second order effect, temperature is measured using an integrated temperature sensor. H_2 sensing accuracy can be increased by incorporating the measured temperature during sensor calibration. An incremental analog to digital converter (ADC) [37] converts the measured temperature and H_2 concentration to 12-bit digital values at different times. Individual Pd nanowires that have between 7 KΩ and 9 KΩ resistance should be biased, with a minimum bias voltage of 50 mV for 10 seconds. These nanowires have been represented by NW_{ref} and NW_{sense} in Figure 9. The voltage around the reference nanowire, $V_R = (V_1 - V_2)$, is used as the reference voltage, while the voltage of the sensing nanowire (V_2) is used as the input voltage for the following incremental ADC in consecutive non-overlapping clock phases. As a 1MHz clock has been used for ADC and since this ADC needs 2^N cycles for N-bits conversion, a 12-bit conversion takes nearly 4 milliseconds. After gas sensing is completed, temperature is measured to further increase the accuracy of gas sensing using an integrated temperature sensor. In the proposed integrated temperature sensor, substrate PNP transistors have been used to generate proportional to absolute temperature (V_{ptat}) and temperature-independent reference (V_{ref}) voltages, and the ADC converts (V_{ptat}/V_{ref}) to a 12-bit digital value. In Figure 9, by using a 50 fF MIM capacitor as C_1 and a 360 fF MIM capacitor as C_2, a temperature-independent reference voltage of approximately 310 mV has been generated. Similar to gas sensing, n-bit digital representation of (V_{ptat}/V_{ref}) is stored in the ADC counter and sent to a wireless transceiver after temperature sensing. The accuracy of temperature sensing is mainly limited by mismatch between Q_1 and Q_2 and nonlinearity in temperature dependence of V_{BE1} and (V_{BE1}- V_{BE2}). Although these errors can be minimized by using dynamic methods presented in [38] to reach ±0.1°C accuracy, such power-consuming techniques are not needed here. The proposed low power temperature sensor can achieve ±1 °C accuracy by only calibrating C_2 and I_{Temp} at room temperature. When the sensor interface circuit operates at a lower frequency, Q_1 and Q_2 transistors are biased with a lower I_{Temp} bias current to reduce the average power consumption of the circuit. Power consumption and conversion time of this ADC can be reconfigured according to the energy stored in the battery to match the amount of available power, resulting in an adaptive, autonomous sensor. The power management circuit dynamically reduces the operating frequency of digital circuits and the bias currents of analog circuits in this sensor interface circuit under reduced light intensity. However, ADC conversion time increases as a result.

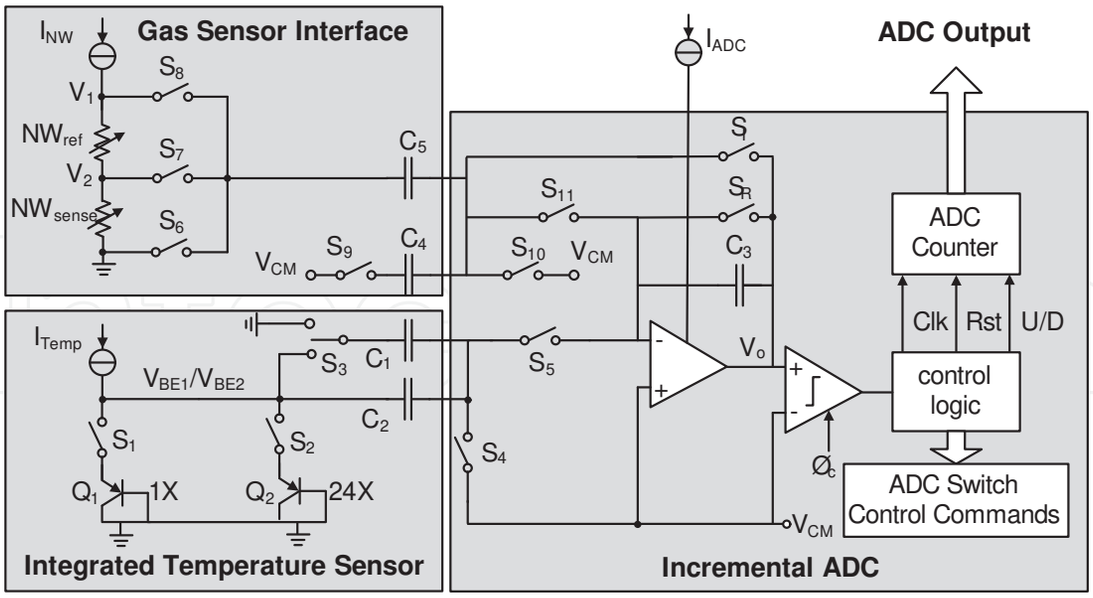

Figure 9. Circuit diagram of the proposed sensor interface [19]

5. Experimental results

The power management and sensor interface circuits have been implemented in a 0.18 μm CMOS process with 0.25 mm^2 total area, as can be seen in the chip microphotograph in Figure 10. The main blocks, including the digital and analog blocks of solar energy harvester and sensor interface circuits, have been specified separately. When operating at 1 MHz, the whole circuit consumes almost 2.1 μW; while the average power consumption of the energy harvester is less than 350 nW. The wireless transceiver sends the measurement results for both temperature and H_2 concentration to a base station every 15 seconds.

Table 4 presents measurement and simulation results for power consumption of the energy harvester and sensor interface circuits in different system operation modes. These operation modes have been defined according to the remaining charge of the battery, which is estimated accurately by detecting the battery voltage between 900 mV and 1.1 V during wireless data transmission, and the battery is discharged by a high current, close to 5 CA. Battery discharge capacity is determined according to the discharge curve of the battery shown in Figure 6. Highly resistive poly resistors have been used in the beta multiplier current source, and oscillator. As these embedded resistors are sensitive to process variations, they have been trimmed initially. If the battery gets discharged, a lower battery voltage is detected during 5 CA discharge and the system is switched to a lower clock frequency to decrease the average power consumption of the whole system. In S_{L2} and S_{L1} modes, the operating frequency is decreased to 500 KHz and 250 KHz, respectively. In S_{L0} mode, when the remaining charge of the battery is less than 25%, the circuit consumes less than 0.6 μW by operating at 125 KHz frequency instead of 1 MHz and using lower bias currents. The average power consumption of the energy harvester drops to less than 110 nW in S_{L0} mode. In addition, measurement results are sent every 120 seconds instead of every 15 seconds in S_{L3} mode, to further reduce the total average power consumption of the whole sensor.

http://dx.doi.org/10.5772/57281

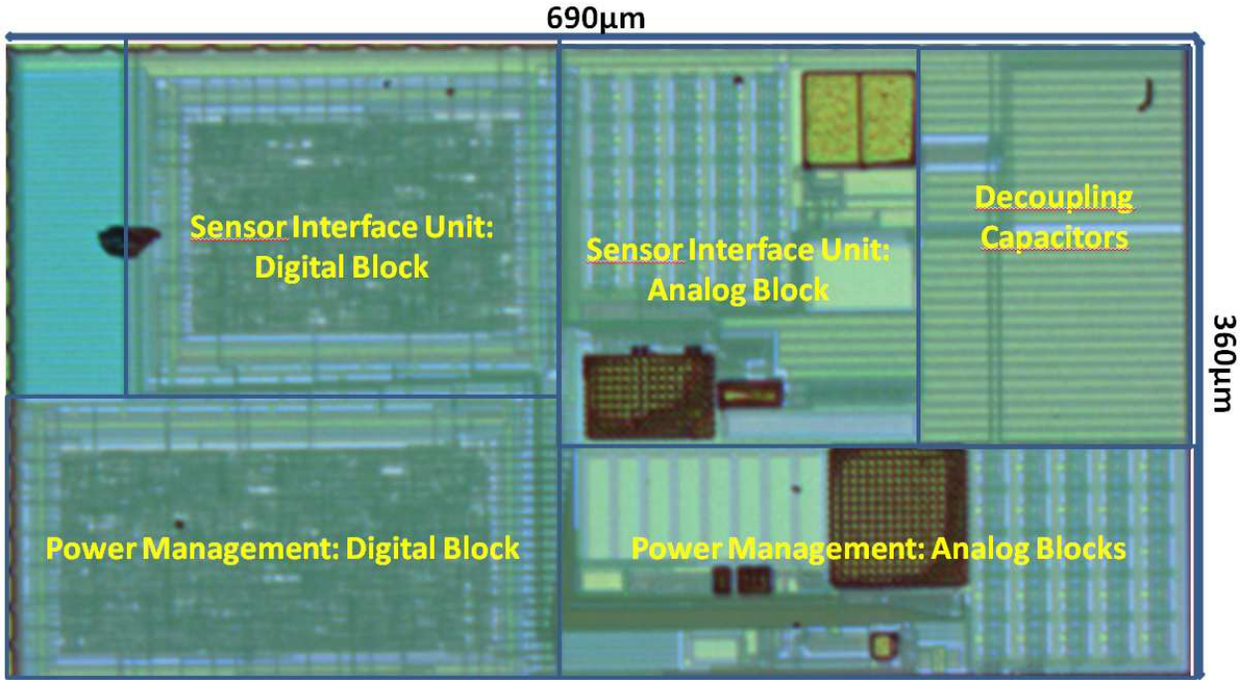

Figure 10. Chip microphotograph of the whole microsystem

Block		S_{L3}	S_{L2}	S_{L1}	S_{L0}
Detected V_{bat} during 5CA discharge (mV)		1104	1051	1002	947
Battery discharge capacity (%)		<20%	<50%	<65%	<75%
Battery threshold voltage (Volt)	Measured	1.114	1.055	1.003	0.955
	Simulated	1.122	1.063	1.010	0.962
Clock frequency (KHz)	Measured	950	488	249	127
	Simulated	980	502	257	132
Time interval of sensing and data transmission (Seconds)		15	30	60	120
Power consumption of clock generator (nW)		165	85	44	23
Power consumption of digital control unit (nW)		90	46	24	13
Average power consumption of energy harvester (nW)	Measured	346	210	142	103
	Simulated	293	169	106	74
Average power consumption of sensor interface circuit (nW)	Measured	1730	1120	790	640
	Simulated	1360	870	625	500
Average power consumption of the integrated circuit (nW)		2076	1330	932	707
Average current consumption of gas sensor bias circuit (µA)		4.67	2.33	1.16	0.58
Average current consumption of the wireless transciever (µA)		9.4	7.7	6.6	5.55
Average current consumption of the complete system (µA)		16	11	8.5	6.7

Table 4. System performance and power consumption in different system operation modes

In order to estimate total power consumption of the sensor, the average power consumption of sensor biasing circuit and wireless transceiver should be calculated. Pd nanowires should be biased with a 7 μA bias current for 10 seconds, before measuring H_2 concentration. TZ1053 consumes 5 μA during standby and consumes 3.3 mA during a period of 20 ms to send a sample with the minimum payload size of 55 bytes [21]. In S_{L3} mode, samples are sent every 15 seconds, and the average current consumption of Pd nanowire sensors and wireless transmission are 4.67 μA and 9.4 μA, respectively. By sending the samples every 120 seconds in S_{L0} mode, these values will be reduced to 0.58 μA and 5.6 μA, respectively. So, the total average current consumption of the whole sensor is less than 16 μA, operating at its highest performance in S_{L3} mode, and is reduced to less than 7 μA, operating in S_{L0} mode.

7. Conclusion

In this chapter challenges in designing energy harvester circuits for miniaturized sensing applications were discussed. Successful implementation of energy harvesting for wireless sensing applications mainly depends on meeting size, autonomy and cost constraints. Miniaturization of WSN platforms can be quite challenging and highly depends on the chosen application and data rate of the transmitted data. Typically the total size of a wireless sensing platform is mainly constrained by the battery and wireless transceiver. In this chapter, system level design challenges, including the selection of appropriate energy storage device and wireless transceiver were discussed. Direct charging approach was presented as an ultra-low power energy-efficient solar energy harvesting approach and a sensing microsystem was also presented for wireless sensing applications.

Author details

Naser Khosro Pour*, François Krummenacher and Maher Kayal

*Address all correspondence to: naser.khosropour@epfl.ch

Ecole Polytechnique Fédérale de Lausanne, Lausanne, Switzerland

References

[1] Vullers, R.J.M.; Schaijk, R.V.; Visser, H.J.; Penders, J.; Hoof, C.V.;, "Energy Harvesting for Autonomous Wireless Sensor Networks," Solid-State Circuits Magazine, IEEE, vol.2, no.2, pp.29-38, Spring 2010

[2] G.-Z. Yang, Ed., Body Sensor Networks. London: Springer-Verlag, 2006

[3] J. Penders, B. Gyselinckx, R. Vullers, M. De Nil, S. Nimmala, J. van de Molengraft, R. Yazicioglu, T. Torfs, V. Leonov, P. Merken, and C. Van Hoof, "Human++: From technology to emerging health monitoring concepts," in Proc. 5th Int. Workshop Wearable and Implantable Body Sensor Networks, Chin. Univ. Hong Kong, China, June 1–3, 2008, pp. 94–98.

[4] T. Sterken, K. Baert, C. Van Hoof, R. Puers, G. Borghs, and P. Fiorini, "Comparative modeling for vibration harvesters," in Proc. IEEE Sensors Conf., 2004, pp.1249–1252.

[5] Lhermet, H.; Condemine, C.; Plissonnier, M.; Salot, R.; Audebert, P.; Rosset, M.;, "Efficient Power Management Circuit: From Thermal Energy Harvesting to Above-IC Microbattery Energy Storage," Solid-State Circuits, IEEE Journal of, vol.43, no.1, pp. 246-255, Jan. 2008

[6] R. J. M. Vullers, H. J. Visser, B. Op het Veld, and V. Pop, "RF harvesting using antenna structures on foil," in Proc. PowerMEMS 2008, Sendai, Japan, Nov. 10–11, 2008, pp. 209–212.

[7] B.W. Cook, S. Lanzisera, K.S.J. Pister, "SoC Issues for RF Smart Dust," Proceedings of the IEEE, vol.94, no.6, pp.1177-1196, June 2006

[8] V. Leonov, T. Torfs, I. Doms, R. F. Yazicioglu, Z. Wang, C. Van Hoof, and R. J. M. Vullers,"Wireless body-powered electrocardiography shirt,"in Proc. Smart Systems Integration, Brussels, Apr. 10–11, 2009, pp. 307–314.

[9] Datasheet Imote 2 (2009). High-performance Wireless Sensor Network Node. [Online]. Available: www.xbow.com

[10] D. Gislason, ZigBee Wireless Networking. London: Newnes Publications, 2008.

[11] Chen, G.; Ghaed, H.; Haque, R.; Wieckowski, M.; Yejoong K.; Gyouho K.; Fick, D.; Daeyeon K.; Mingoo S.; Wise, K.; Blaauw, D.; Sylvester, D. A cubic-millimeter energy-autonomous wireless intraocular pressure monitor. ISSCC, pp.310-312, Feb. 2011

[12] Chen, G.; Hanson, S.; Blaauw, D.; Sylvester, D.;, "Circuit Design Advances for Wireless Sensing Applications," Proceedings of the IEEE, vol.98, no.11, pp.1808-1827, Nov. 2010

[13] Qiu, Y., Liempd, C.V., Veld, B.O.H., Blanken, P.G., Hoof, C.V.: '5μW-to-10mW input power range inductive boost converter for indoor photovoltaic energy harvesting with integrated maximum power point tracking algorithm', ISSCC, pp.118-120, Feb. 2011

[14] Hui, S., Chi-Ying, T., Wing-Hung, K.: 'The Design of a Micro Power Management System for Applications Using Photovoltaic Cells With the Maximum Output Power Control', IEEE Tran. VLSI Systems, vol.17, no.8, pp.1138-1142, Aug. 2009

[15] Jungmoon, K., Jihwan, K., Chulwoo, K.: 'A Regulated Charge Pump With a Low-Power Integrated Optimum Power Point Tracking Algorithm for Indoor Solar Ener-

gy Harvesting', IEEE Tran. Circuits and Systems II: Express Briefs, vol.58, no.12, pp. 802-806, Dec. 2011

[16] Khosro Pour, N.; Krummenacher, F.; Kayal. M. Fully integrated ultra-low power management system for micro-power solar energy harvesting applications. Electronics Letters, vol. 48, p. 338-U118, 2012.

[17] M. Kayal, F. Vaucher and Phi. Deval, "New Error Amplifier Topology for Low Dropout Voltage Regulators Using Compound OTA-OPAMP," Proceedings of the 32nd European Solid-State Circuits Conference, ESSCIRC 2006, pp.536-539, Sept. 2006

[18] Khosro Pour, Naser; Facchin, Stefano; Krummenacher, Francois; Kayal, Maher;, "An ultra-low power li-ion battery charger for micro-power solar energy harvesting applications," Electronics, Circuits and Systems (ICECS), 2012 19th IEEE International Conference on, vol., no., pp.516-519, 9-12 Dec. 2012

[19] Pour, N.K.; Krummenacher, F.; Kayal, M. Fully Integrated Solar Energy Harvester and Sensor Interface Circuits for Energy-Efficient Wireless Sensing Applications. J. Low Power Electron. Appl. 2013, 3, 9-24.

[20] Offermans, P.; Tong, H. D.; Van Rijn, C. J. M.; Merken, P.; Brongersma, S. H.; Crego-Calama, M. Ultralow-power hydrogen sensing with single palladium nanowires. Applied Physics Letters, vol.94, no.22, pp.223110-223110-3, Jun 2009

[21] N. Khosro Pour, F. Krummenacher and M. Kayal. A miniaturized autonomous microsystem for hydrogen gas sensing applications, New Circuits and Systems Conference (NEWCAS), 2012 IEEE 10th International, vol., no., pp.201-204, 17-20 June 2012

[22] TZ1053 Datasheet [Online] Available: www.toumaz.com

[23] CC2520 Datasheet [Online] Available: www.ti.com

[24] CC2570 Datasheet [Online] Available: www.ti.com

[25] GZ115F Datasheet [Online]. Available: http://www.cap-xx.com

[26] MEC220 Datasheet [Online]. Available: http://www.infinitepowersolutions.com

[27] CBC050 Datasheet [Online]. Available: http://www.cymbet.com

[28] Varta V6HR Datasheet. [Online]. Available: http://www.varta-microbattery.com

[29] Chao, Lu; Raghunathan, V.; Roy, K. Micro-scale energy harvesting: A system design perspective, Design Automation Conference (ASP-DAC), 2010 15th Asia and South Pacific, vol., no., pp.89-94, 18-21 Jan. 2010

[30] Jia, G.; Steglich, M.; Sill, I.; Falk F. Core–shell heterojunction solar cells on silicon nanowire arrays. Solar Energy Materials and Solar Cells, Vol.96, Jan. 2012, Pages 226-230, ISSN 0927-0248

[31] Esram, E.; Chapman, P. L. Comparison of photovoltaic array maximum power point tracking techniques. IEEE Transactions on Energy Conversion, vol. 22, No. 2, pp. 439-449, June, 2007

[32] Chao, Lu; Raghunathan, V.; Roy, K. Maximum power point considerations in micro-scale solar energy harvesting systems. Circuits and Systems (ISCAS), Proceedings of 2010 IEEE International Symposium on, vol., no., pp.273-276, May 30 2010-June 2 2010

[33] Pastre, M.; Krummenacher, F.; Kazanc, O.; Khosro Pour, N.; Pace, C.; Rigert, S.; Kayal, M. A solar battery charger with maximum power point tracking. 18th IEEE International Conference on Electronics, Circuits and Systems (ICECS) 2011, pp.394-397, 11-14 Dec. 2011

[34] Pastre, M.; Krummenacher, F.; Robortella, R.; Simon-Vermot, R.; Kayal, M. A fully integrated solar battery charger. Joint IEEE North-East Workshop on Circuits and Systems and TAISA Conference, NEWCAS-TAISA 2009, pp.1-4, June 28 2009-July 1 2009

[35] Zarlink ZL70250 Datasheet. [Online]. Available: http://www.zarlink.com/zarlink

[36] Van der Bent, J.F.; Van Rijn, C.J.M. Ultra low power temperature compensation method for palladium nanowire grid. Procedia Engineering, vol. 5, 2010, pp. 184-187

[37] Pertijs, M.A.P.; Makinwa, K.A.A.; Huijsing J.H. A CMOS smart temperature sensor with a 3σ inaccuracy of ±0.1°C from -55°C to 125°C. IEEE Journal of Solid-State Circuits, vol.40, no.12, pp. 2805- 2815, Dec. 2005

[38] Markus, J.; Silva, J.; Temes, G.C. Theory and applications of incremental ΔΣ converters. IEEE Transactions on Circuits and Systems I: Regular Papers, vol.51, no.4, pp. 678- 690, April 2004

[39] Koshro-Pour, N.; Kayal, M.; Jia, G.; Eisenhawer, B.; Falk, F.; Nightingale, A.; De Mello, J.C; et al. "A miniaturised autonomous sensor based on nanowire materials platform: the SiNAPS mote." In SPIE Microtechnologies, pp. 87631Q-87631Q. International Society for Optics and Photonics, 2013.

IntechOpen